The Effects of Iron and Manganese Doping on the Carbonation of Brucite [$Mg(OH)_2$]

Dong Youn Chung*[1], Juliane Weber[1], Lawrence M. Anovitz[1], Barbara R. Evans[1], Ke Yuan[1], Sai Adapa[1], Matthew G. Boebinger[2], Michael A. McGuire[3], Raphaël P. Hermann[3], George Yumnam[3], Joanne E. Stubbs[4], Peter J. Eng[4,5], Peter J. Heaney[6], Andrew G. Stack*[1]

[1] Chemical Sciences Division, Oak Ridge National Laboratory, Oak Ridge, TN 37830
[2] Center for Nanophase Materials Sciences, Oak Ridge National Laboratory, Oak Ridge, TN 37830
[3] Materials Science and Technology Division, Oak Ridge National Laboratory, Oak Ridge, TN 37830
[4] Center for Advanced Radiation Sources, The University of Chicago, Chicago, IL 60637
[5] James Franck Institute, The University of Chicago, Chicago, IL 60637
[6] Department of Geosciences, Penn State University, University Park, PA 16802

*Corresponding author: stackag@ornl.gov, chungd@ornl.gov

Keywords: Carbon dioxide removal, mineral looping, $Mg(OH)_2$ (brucite), direct air capture via enhanced weathering, metal impurities, carbon sequestration

Submitted to *The Journal of Physical Chemistry C*

Abstract

Brucite [$Mg(OH)_2$] is a promising sorbent for carbon dioxide removal (CDR) due to its availability and low calcination temperatures. However, natural and synthetic brucites tend to contain metal impurities, such as iron or manganese, and how these impurities affect the interfacial chemical reactivity is uncertain. Here, the impact of low concentrations of iron and manganese impurities on the carbonation efficiency of $Mg(OH)_2$ was examined. $Mg(OH)_2$ with small amounts (1-5 mol%) of Fe and Mn was synthesized. The increasing substitution of Fe into $Mg(OH)_2$ was accompanied by the oxidation of Fe. The phase transformation sequence during the carbonation was found to be: brucite [$Mg(OH)_2$] → amorphous magnesium carbonate ($MgCO_3 \cdot nH_2O$) → nesquehonite ($MgCO_3 \cdot 3H_2O$), regardless of impurity concentration. Both the Fe- and Mn-doped $Mg(OH)_2$ samples were more reactive than end-member $Mg(OH)_2$, possibly due to their higher surface areas and lower stabilities. During carbonation, 3 mol% Fe- and Mn-doped $Mg(OH)_2$ showed the highest reactivity. The variance in reactivity for Mn-doped $Mg(OH)_2$ was less than that of Fe-doped $Mg(OH)_2$. These results suggest that natural or industrial waste $Mg(OH)_2$ with less than 5 mol% Fe and Mn impurities may be targeted as more effective CDR sorbents than endmember $Mg(OH)_2$.

51

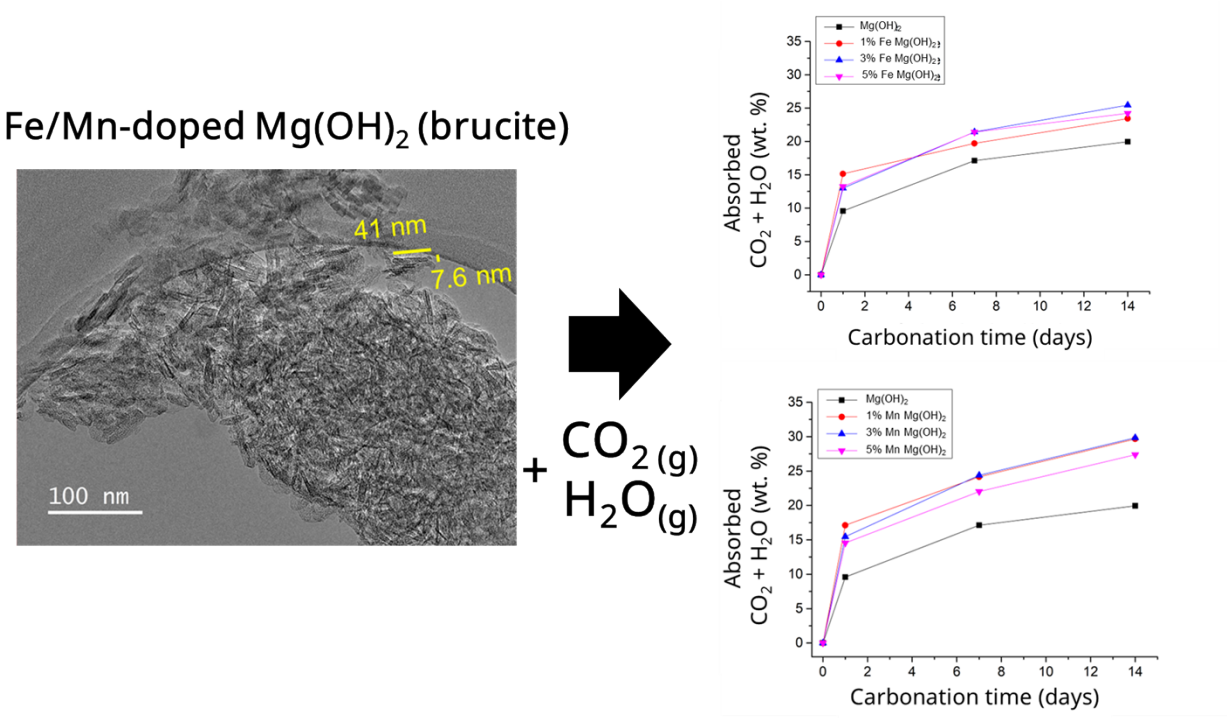
Fe/Mn-doped Mg(OH)2 (brucite)
41 nm
7.6 nm
100 nm
+
CO2 (g)
H2O(g)
Mg(OH)2
1% Fe Mg(OH)2
3% Fe Mg(OH)2
5% Fe Mg(OH)2
Absorbed CO2 + H2O (wt. %)
Carbonation time (days)
Mg(OH)2
1% Mn Mg(OH)2
3% Mn Mg(OH)2
5% Mn Mg(OH)2
Absorbed CO2 + H2O (wt. %)
Carbonation time (days)

52

53

1. Introduction

Calcium and magnesium oxides (CaO/MgO) have displayed great promise as economic agents for large-scale removal of CO_2 from the atmosphere.[1–7] The basic concept is to react these oxides with atmospheric CO_2, forming calcium/magnesium carbonates and fixing the CO_2 as CaO/ $MgO + CO_2 \rightarrow CaCO_3/MgCO_3 \cdot nH_2O$.These carbonates are then calcined to regenerate the sorbent and separate the CO_2, which can be injected in the subsurface[8] or converted to other products[9,7,10]: $CaCO_3/MgCO_3 \cdot nH_2O \rightarrow CaO/MgO + CO_2 + nH_2O$. The magnesium-based system has both disadvantages and advantages for carbon dioxide removal (CDR) over the calcium-based system[10]. Available data suggest that CaO carbonates faster than MgO, but CaO may suffer from surface armoring that slows carbonation[11]. The calcination temperature of magnesite ($MgCO_3$) to periclase (MgO) is lower (400 °C) than that of calcite ($CaCO_3$) to lime (650 °C)[12,13,10]. In fact, the carbonated product of MgO is often a hydrated magnesium carbonate, such as nesquehonite ($MgCO_3 \cdot 3H_2O$), hydromagnesite ($Mg_5(CO_3)_4(OH)_2 \cdot 4H_2O$), or dypingite ($Mg_5(CO_3)_4(OH)_2 \cdot 5\text{-}8H_2O$)[14], whose decarbonation temperatures are still lower than that of calcite[15,16,17]. Furthermore, MgO has a high theoretical carbon capture efficiency (1.09 g CO_2 per gram of MgO)[18–20]. What isn't clear is if the detrimental interfacial chemical reactivity of MgO can be bypassed to make it a more favorable substrate for CDR than CaO.

If magnesium phases are to be used for CDR, the starting material needs to be optimized. Although brucite [$Mg(OH)_2$] is a relatively rare mineral[21], it nevertheless has advantages over periclase (MgO) in terms of availability. Moreover, the reaction of brucite with CO_2 is rapid at low temperatures. Brucite occurs as a low-temperature hydrothermal alteration product through metamorphism, as either a primary product or a byproduct[22], whereas periclase often hydroxylates to brucite at the earth's near surface[23]. Brucite also occurs as a waste mineral in ultramafic mining

77 and processing, and its abundance has been estimated in the range of ~1 to 15 weight percent of
78 chrysotile tailings, nickel tailings and deposits, and chromite ore processing residue[24–28]. Brucite
79 also can be generated from Mg-containing natural/industrial brines[29–31].

80 In addition, the conversion of MgO to $Mg(OH)_2$ is relatively fast in the presence of water.
81 For MgO powder, it has been reported that full hydration occurred in 400 minutes at 38 °C[26].
82 Therefore, every source of periclase, such as from the decarbonation of magnesite ($MgCO_3$), from
83 a mixed Ca/Mg oxide derived from the decarbonation of dolomite ($CaMg(CO_3)_2$)[32], or the
84 extraction of Mg from Mg silicate[33], can be a possible source of $Mg(OH)_2$ as well. In fact, when
85 Mg is extracted from Mg silicate, using brucite as a CDR sorbent will be beneficial in terms of
86 energy and associated CO_2 emissions by eliminating the calcination step of $Mg(OH)_2$ to MgO.
87 Also, in the case of mineral looping, the deactivation of sorbent due to surface area decrease[34–38]
88 could be addressed by hydration-induced fracturing[39] during the transformation of MgO to
89 $Mg(OH)_2$, providing an additional advantage to maintaining the carbonation rate after multiple
90 looping cycles[40]. The rates of dissolution reactions are often proportional to surface area[41,42], which
91 can become self-limiting when armoring or passivation occur since these reduce the reactive
92 surface area[11]. The surface area can be increased by reaction-induced fracturing[43] when MgO is
93 converted to $Mg(OH)_2$, resulting in a volume expansion of 110 %[39,44].

94 Another advantage of using brucite in CDR is that water vapor concentration enhances the
95 carbonate reaction rate and extent, in the form of high relative humidities[45–47]. It has been proposed
96 that the reaction mechanism of MgO to magnesium carbonate (hydrate) consists of three steps[10]:
97 1) fast transformation of MgO to $Mg(OH)_2$; 2) the rate limiting dissolution of $Mg(OH)_2$; and 3)
98 precipitation of magnesium carbonate (often in a hydrated form). This reaction chain may not be
99 as linear as proposed because it has been observed that a MgO crystal exposed to air forms a

100 complex mixture of $Mg(OH)_2$ and various Mg-carbonates[11]. Therefore, using $Mg(OH)_2$ as a
101 starting material will only improve carbonation kinetics if $Mg(OH)_2$ dissolution is not rate limiting.

102 Naturally-sourced brucite often has metal impurities, and the most common metal
103 impurities in natural brucite are Fe and Mn[48–55]. For example, natural brucite may contain Fe(II)
104 from less than 5 mol % to up to 60 mol% in highly reduced conditions[50,51]. Other sources of Mg
105 also often contain metal impurities. Further, the natural sources from which Mg may be reacted to
106 brucite typically contain metal impurities. Fe and Mn are common in source rocks for Mg[56], and
107 Mg-containing brines also have various metal impurities[57,58]. Indeed, these pathways may serve as
108 a primary source of brucite for CDR. Consequently, it is quite possible that metal impurities will
109 be present in any $Mg(OH)_2$-brucite used as a CDR sorbent, regardless of its origin. Therefore,
110 understanding the effect of metal impurities on the interfacial reactions that determine the
111 carbonation efficiency of $Mg(OH)_2$ is critical in evaluating the practicality of using brucite as a
112 CDR sorbent.

113 Previous studies have shown that the products of carbonation of Fe-doped $Mg(OH)_2$ can
114 be Mg hydroxy-carbonates and Fe (hydr)oxides[59,60]. Vessey et al. (2024) reported decreasing
115 carbonation efficiency with increasing Fe(II) content in $Mg(OH)_2$ under both oxic and anoxic
116 conditions when the Fe concentration is higher than 6 mol%[59]. Likewise, Boschi et al. (2017)
117 suggested that the spontaneous CO_2 uptake by natural serpentinized ultramafic rocks is higher for
118 Fe-poor brucite with ~4 mol% Fe than for Fe-rich brucite with up to 20 mol% Fe[22]. On the other
119 hand, Weber et al. (2025)[61] observed increased carbonation efficiency when the formation of nano-
120 scale iron oxides was accompanied during the hydration of MgO with 0.001-0.1 M of dissolved
121 $FeCl_2$. Thus, whereas high concentrations of Fe impurities appear to inhibit the carbonation of
122 brucite, the effect of low concentrations of Fe impurities that characterize most sources of Fe-

123 doped brucite is still poorly understood. In addition, although Mn is the second most common
124 minor impurity in $Mg(OH)_2$, to the best of our best knowledge, no previous studies focus on the
125 effect of Mn impurities on the carbonation of brucite. Therefore, the effects of low concentration
126 ($\leq$ 5 mol%) Fe and Mn impurities on $Mg(OH)_2$ carbonation require further analysis.

127 This investigation evaluates the effects of low concentration doping (1, 3, and 5mol%) of
128 Fe and Mn in $Mg(OH)_2$ on carbonation. We propose that low concentrations of Fe and Mn
129 impurities improve the carbonation efficiency of brucite by modifying the sorbent surface area and
130 stability. This study contributes to evaluations of the utility of brucite [$Mg(OH)_2$] with low
131 concentrations of Fe and Mn impurities as a CDR sorbent.

132

133 ## 2. Methods

134 **2.1. Nano-brucite [$Mg(OH)_2$] Synthesis.** Nano-$Mg(OH)_2$ was synthesized according to
135 the protocols of Hadia et al. (2015)[62]. To confirm that differences in size, surface area, and
136 morphology do not stem from differences in synthesis method, endmember $Mg(OH)_2$ was also
137 synthesized using the co-precipitation approach (Method S1).

138 ### 2.1.1. Synthesis of endmember nano-$Mg(OH)_2$

139 42.0 g of NaOH pellets were dissolved in a solution containing 490 mL of 1:1 ethanol and
140 deionized water with a magnetic stir bar at 700 rpm. After NaOH pallets were fully dissolved,
141 24.1 g of solid $Mg(NO_3)_2 \cdot 6H_2O$ were directly placed in the stirred NaOH solution. This solution
142 was stirred for 3 hours. After that, the stirring was turned off and precipitates were left to settle
143 overnight. The clean supernatant was decanted, and precipitates were evenly dispensed to six

50 mL centrifuge tubes. They were centrifuged at 12,000 rpm for 10 minutes four times at room temperature and 30 minutes for the last time. After each centrifugation cycle, the supernatant was decanted, and deionized water was added to almost fill the tubes (~40 mL) to remove residual salts and base. The precipitates were consolidated to reduce the number of centrifuge tubes before the second, fourth, and fifth cycles. After the fifth cycle, the supernatant was decanted, and the precipitate was dried in a vacuum oven at -19.2 psi relative to room pressure and ~75°C. After drying for three days, the precipitates were gently ground using an agate mortar.

2.1.2. Synthesis of Fe- and Mn-doped nano-$Mg(OH)_2$

The Fe- and Mn-doped nano-$Mg(OH)_2$ were synthesized using reagent grade $FeCl_2 \cdot 4H_2O$ powder (≥99.0%, Sigma-Aldrich) and $MnCl_2$ pellets (99.998%, Alfa Aesar) as a dopant, respectively. To prevent oxidation of Fe^{2+} and Mn^{2+}, the synthesis of Fe- and Mn-doped $Mg(OH)_2$ was conducted in a Schlenk line. The air in the Schlenk line was pumped out and Ar gas was flowed to an overpressure of ~5 psi. All solvents were 1:1 ethanol (HPLC grade, Supelco®) and deionized water solution. 7.38 g of $Mg(NO_3)_2 \cdot 6H_2O$ (99%, Sigma-Aldrich) were dissolved in 50 mL of the solvent in the Schlenk line and stoichiometric amounts of $FeCl_2 \cdot 4H_2O$ or $MnCl_2$ were dissolved in the Schlenk line to make 1, 3, and 5 mol% Fe- or Mn-doped $Mg(OH)_2$. 50 mL of solvent was added into the Schlenk line to dissolve any reagent stuck on its walls. The solution was stirred during the entire synthesis at 1200 rpm. 12.875 g of NaOH pellets (≥98.0%, Sigma-Aldrich) were dissolved in 100 mL of the solvent in a separate beaker that was exposed to the atmosphere. When there was no visible solute left, the NaOH solution was mixed into the Mg and metal dopant-containing solution in the Schlenk line, with constant stirring. As soon as the NaOH solution was added, the solutions become opaque with a light blue color for Fe-containing solutions, and pink for Mn-containing solutions. The stirring was stopped and precipitates were

left to settle overnight; however, there was no visible separation between the precipitate and supernatant. To prevent oxidation of Fe^{2+} or Mn^{2+}, the solution was evenly dispensed into 50 mL centrifuge tubes and centrifuged at 12,000 rpm for 10 minutes five times, except for the fifth centrifuge cycle of the 1 mol% Fe-doped $Mg(OH)_2$ (which was centrifuged for 30 minutes). After each centrifuge cycle, while in the glove box (MBraun LABmaster SP, ~ 5 bar N_2, < 0.1 ppm H_2O, < 5 ppm O_2), the supernatant was decanted, and deionized water was added and mixed to remove residual salts and bases. The precipitates were merged to reduce the number of centrifuge tubes after each cycle until all products were in one centrifuge tube. After the final centrifuge cycle, the supernatant was decanted, and the precipitate was dried in a vacuum oven in the glove box at 70°C for 10 hours. After drying, we observed the color of the precipitates changed to light yellow (1 mol% Fe) to orange (5 mol% Fe), and light blue (1 mol% Mn) to dark pink (5 mol% Mn). The dried powders were gently ground with a mortar in the glove box. The Fe- and Mn-doped $Mg(OH)_2$ was always stored in a glove box except during the analysis or carbonation experiments.

2.2. Conventional XRD. A Panalytical X-ray diffraction (XRD) instrument with a Cu$K\alpha$ ($K_{\alpha 1}$=1.5406 Å, $K_{\alpha 2}$=1.5444 Å) source and a PIXcel3D 1x1 detector was used to identify synthesis and carbonation products. The samples were scanned from 5° to 90° 2θ in 10 minutes with a 0.03° resolution at an operating voltage of 45 kV and an operating current of 40 mA. There were no observable color changes of Fe, Mn-doped brucites during the measurement.

2.3. Synchrotron XRD and Rietveld refinement. Synchrotron X-ray diffraction of endmember and Fe- (1 and 5 mol%), and Mn-doped (3 and 5 mol%) $Mg(OH)_2$ powders was conducted at the GeoSoilEnviroCARS (GSECARS) Beamline 13BMC at the Advanced Photon Source (APS), Argonne National Laboratory. Rietveld structure refinements[63] of the synchrotron

XRD patterns were conducted using the General Structure Analysis System-II (GSAS-II) software[57]. The detailed process is described in Method S2.

2.4. SEM. A ZEISS Gemini SEM field emission-scanning electron microscope (FE-SEM) was used to study the size and morphology of the materials. Powder samples were mounted on carbon tape attached to SEM stubs. The electron accelerating voltage was 1 kV and a secondary electron detector was used.

2.5. TEM. Transmission electron microscope (TEM) bright field images were collected using a Titan TEM at an operating voltage of 300 kV. The TEM samples were prepared by mixing a small amount of $Mg(OH)_2$ powder in isopropanol, sonicating for 10 minutes, putting 10 µL of the mixture on a lacey carbon grid, and evaporating the isopropanol at room temperature.

2.6. BET Surface Area Measurement. Brunauer-Emmett-Teller (BET)[65] surface area analyses were conducted with a Micromeritics BET analyzer. Several milligrams of each sample were placed in a BET tube after measuring the empty tube mass. The samples were then degassed on a SmartVacPrep instrument (Micromeritics, Norcross, GA, USA) with heating mantles at 150℃ for 12 hours. After the degassing, the mass of the tube was measured to calculate the dried sample mass. BET measurements were conducted at liquid N_2 temperature with a nitrogen adsorbate.

2.7. TGA-MS Analysis. Thermogravimetric-Mass Spectrometry Analyses (TGA-MS) of the as-synthesized and carbonated powders were conducted with a TA Instruments TGA 5500 (Weighing Precision: ±0.01 %, Resolution: <0.1 µg, Temperature Precision: ±0.1 °C) coupled with a Discovery mass spectrometer under flowing Ar gas at 10℃/minute up to 700℃.

2.8. ICP-OES Analysis of Metal Content. To confirm the uptake of the dopants by $Mg(OH)_2$, the end-member and Fe-/Mn-doped powders were dissolved in 2 M nitric acid, while Mn-doped powders were dissolved in 2 M nitric,1 and 6 M hydrochloric acid solutions. The metal contents of the aqueous solutions were determined by Inductively Coupled Plasma-Optical Emission Spectroscopy (ICP-OES) using an iCAP 7000 spectrometer (Thermofisher Scientific) equipped with a prepFast M5X automatic dilution automatic sample loader (Elemental Scientific, Omaha, Nebraska). The detailed analysis process is described in SI, Method S3.

2.9. Mössbauer Spectroscopy. Three 80 mg samples of Fe-doped $Mg(OH)_2$ with nominal Fe concentrations of 1, 3, and 5 mol% were utilized for Mössbauer spectroscopy measurements. The samples were sealed between two layers of Kapton tape, protecting them from further exposure to the air. In each series, the source was ^{57}Co@Rh, with 5 mCi activity. For room temperature measurements, a Kr gas proportional counter set to collect the 14.4 keV radiation and the Kr escape peak was utilized; the drive was calibrated using α-Fe foil, which serves as the isomer shift reference, in the ±4 mm/s velocity range. For measurements at 10 K, a Janis SHI-850 closed cycle cryostat and a Ritverc-2 Tl@NaI scintillator were utilized; the same calibration procedure was used in the ±12 mm/s velocity range.

2.10. *Ab initio* Molecular Dynamics Modeling of Starting Fe and Mn $Mg(OH)_2$. *Ab-initio* molecular dynamics (AIMD) modeling was conducted to estimate the stability of the Fe- and Mn- doped $Mg(OH)_2$. The AIMD simulations were performed with CP2K/Quickstep package using the Perdew-Burke-Ernzerhof (PBE)[66] functional with a hybrid Gaussian plane wave. The detailed simulation setup is described in Method S4.

2.11. Magnetometry. Magnetization measurements were carried out using the vibrating sample magnetometer (VSM) option in a Magnetic Property Measurement System 3 (MPMS3) from Quantum Design. The powder sample was loaded into an air-tight plastic capsule, preventing further exposure to the air, which was then mounted in a brass holder. Temperature-dependent data were collected on warming. No difference was observed for data collected after cooling the sample in the applied field and cooling the sample in a zero field. Isothermal magnetization data were collected at 300 and 2 K (full loops between 60 kOe and -60 kOe).

2.12. Carbonation Experiments. Carbonation of the endmember and Fe-, Mn-doped $Mg(OH)_2$ was conducted using a custom-built multi-vessel system[67] at 100% relative humidity (Fig. S9). Three glass vials, open at the top, containing synthetic $Mg(OH)_2$ powder (~150-250 mg) were placed in a Teflon-lined reaction vessel and connected to a CO_2 tank. For endmember $Mg(OH)_2$, the three vials were filled with the $Mg(OH)_2$ powder, but for the 1, 3, and 5 mol% Fe- and Mn-doped $Mg(OH)_2$, the powders were placed in each vial and carbonated in the same vessel. Since the ambient CO_2 pressure may limit the diffusion rate of CO_2 into the powers[68], the carbonation experiment was conducted at 1 bar CO_2 above atmospheric pressure (gauge). To maintain a constant relative humidity, approximately 2 mL of deionized water was placed at the bottom of the Teflon reaction cell, around the glass vials but not in direct contact with the powder. Each sample was carbonated at room temperature for 1, 7, and 14 days. After carbonation, the samples were dried at room temperature under vacuum at ~-20 psi overnight and then placed in sample containers. The metal-doped samples were stored in a glove box to limit oxidation.

3. Results

3.1. Synthetic Powder Characterization. The synthetic $Mg(OH)_2$ powders were characterized by XRD to identify phases, ICP-OES for metal content, BET for surface area, and Mössbauer spectroscopy and magnetometry to identify the iron oxidation states and magnetic properties. These techniques were also employed to determine whether any nano-scale iron oxides had formed.

3.1.1 Structure and composition of Fe- and Mn-Doped $Mg(OH)_2$. XRD revealed only monophasic brucite for all samples (Fig. 1 (A), (C)). However, the peak positions for Fe-doped $Mg(OH)_2$ were shifted to slightly lower 2θ relative to endmember $Mg(OH)_2$, indicating an expanded unit cell. In addition, the peak widths for Fe- and Mn-doped $Mg(OH)_2$ were broader than those for endmember $Mg(OH)_2$, especially for peaks that contain *c*-axis contributions (Fig. 1 (A) and (B), Fig. S2, Table S5). This broadening may reflect either a smaller crystallite size for Fe-doped $Mg(OH)_2$ (Fig. 1 (B)) or a structural distortion caused by the substitution of Fe for Mg. Mn-doped $Mg(OH)_2$ also exhibited a unit-cell expansion and peak broadening relative to endmember $Mg(OH)_2$. The asymmetric (00*l*) peaks observed in synchrotron XRD patterns of the Fe- and Mn-doped $Mg(OH)_2$ (Fig. S2) suggest some turbostratic disorder of the trioctahedral sheets[69,70].

Rietveld refinements confirmed that the lattice parameters for Fe- and Mn-doped $Mg(OH)_2$ were larger than those for endmember $Mg(OH)_2$, especially along the *c*-axis (Table S1, Fig. S2). The refined crystallite sizes were similar to the particle sizes observed using SEM and TEM (Fig. S4 (B) and Fig. 1 (B), (D)). We refined occupancies for Fe and Mn in the metal sites in the octahedral sheets with the constraint that Fe and Mg (or Mn and Mg) must sum to unity. The Rietveld fitting yielded occupancies for Fe and Mn close to the concentrations measured by ICP-OES (Tables S1, S2, S4), strongly suggesting that Fe and Mn are substituting within the octahedral sites.

The Fe concentrations for the doped $Mg(OH)_2$ were measured by ICP-OES to be 0.8, 2.9, and 4.8 mol%, for the nominally 1, 3 and 5 mol% Fe-doped $Mg(OH)_2$, respectively (Table S2). The Mn concentrations for the nominally 1, 3, and 5 mol% Mn-doped $Mg(OH)_2$ were 1.0, 2.9, and 5.0 mol%, respectively (Table S3). Although the Fe and Mn may precipitate as an amorphous secondary phase, it is unlikely that a crystalline secondary phase formed as none was detected by the synchrotron XRD analysis (Fig. S2). Likewise, no crystalline or amorphous Fe/Mn (hydr)oxides were observed by TEM.

3.1.2. Particle Size and Morphology. The Fe- and Mn-doped $Mg(OH)_2$ exhibited some quantitative differences from endmember $Mg(OH)_2$. The average size of the Fe- (Fig. 1 (B), Fig. S3) and Mn-doped $Mg(OH)_2$ (Fig. 1 (D), Fig. S3) particles were smaller (~8 nm × 40 nm), with a surface area that was 2-3 times higher than that of endmember $Mg(OH)_2$ (Fig. S4 (B), Table S6). In addition, the Fe- and Mn-doped $Mg(OH)_2$ displayed a mostly acicular (needle-like) morphology, whereas endmember $Mg(OH)_2$ formed as hexagonal platelets. This disparity in habits suggests that Fe or Mn in either the octahedral sites or the interlayer causes stresses that force the $Mg(OH)_2$ to curl. Such curling due to internal strain has been observed in clay minerals with a dimensional mismatch between tetrahedral and octahedral sheets (e.g. halloysite or chrysotile nanotubes) [69,70]. The sizes, morphologies, and BET surface areas of endmember $Mg(OH)_2$ synthesized by the addition of solid (Method S1.1) were similar to those for endmember $Mg(OH)_2$ synthesized by co-precipitation (Fig. S4). Thus, we conclude that the acicular habits of the Fe- and Mn-doped $Mg(OH)_2$ can be attributed to the metal impurities, rather than the synthesis method.

3.1.3. Oxidation State of Fe in Fe-doped $Mg(OH)_2$. Although significant efforts were undertaken during synthesis to keep the iron and manganese in the divalent state by maintaining an anoxic environment, color variations during the drying process suggested that some oxidation

299 did occur. To test the oxidation state of Fe, we conducted room-temperature Mössbauer analyses.
300 The Fe-doped $Mg(OH)_2$ samples exhibited some variations in their Mössbauer spectra, but it is
301 clear that much of the Fe in the $Mg(OH)_2$ was ferric (Fig. 2). Indeed, there was no visible Fe(II)
302 peak in the 5 mol% Fe-doped sample. Although surprising, the presence of only Fe(III) in the 5
303 mol% Fe-doped $Mg(OH)_2$ is consistent with the pyrophoric behavior of endmember $Fe(OH)_2$[73].
304 For the 1 and 3 mol% Fe-doped samples, a clear Fe(II) line was visible at 2.6 mm/s. Unfortunately,
305 this line cannot be unequivocally associated with a second, expected line at ~ -0.5 mm/s to form a
306 Fe(II) doublet. However, in analyzing the spectral parameters for Fe in $Mg(OH)_2$, Binfu et al.[74]
307 found different linewidths for the lines at 2.592(2) and -0.304(2) mm/s. Thus, to avoid overfitting
308 the data, we utilized their exact model (d = 1.144 and quadrupole splitting ΔE_Q = 2.895mm/s) for
309 the room temperature data. These parameters fit the Fe(II) line at 2.6 mm/s very well. The Fe(II)
310 component was, thereby, found to be 18(5) and 19(2) mol% of the total iron for the 1 and 3 mol%
311 Fe-doped samples, respectively. The detailed fitting procedure is described in Result S1.

312 The low-temperature Mössbauer spectroscopy at 10 K (Fig. S6) and magnetometry down
313 to 2 K (Result S2, Fig. S7) both indicate that 5 mol% Fe-doped $Mg(OH)_2$ is paramagnetic at room
314 temperature and non-magnetic even at the base temperature (2 K). This result indicates the
315 presence of unpaired electrons in the Fe, consistent with the valence state as Fe(III). There was no
316 magnetic splitting observed in the low-temperature Mössbauer spectra. The spectral
317 decomposition (Fig. S6) is not unique but is compatible with that for room temperature. A broad
318 Fe(III) component in the 1 mol% Fe-doped sample at room temperature appeared somewhat
319 sharper at 10 K, though this is at the edge of the data statistics, as the signal is fairly small.

320 In their Mössbauer analyses of natural brucites, Blaauw et al.[75] found that the divalent and
321 trivalent Fe content varied with locale. Binfu and Yilong[74] observed a dominant divalent Fe

doublet with a secondary trivalent doublet in natural Fe-brucite. The difference in the ferrous/ ferric iron ratio between the synthetic sample (this study) and natural samples[74,75] is likely due to differences in formation pathways and the distribution of impurities.

3.1.4. Dehydration Behavior of Endmember and Doped $Mg(OH)_2$. During the TGA-MS analysis, the dehydration of Fe- and Mn-doped $Mg(OH)_2$ occurred at a lower temperature (~320-360℃) than endmember $Mg(OH)_2$ (~375℃), suggesting that the substitution of Fe and Mn destabilizes $Mg(OH)_2$ (Fig. S5). The Fe-doped $Mg(OH)_2$ did not reveal a trend between dehydration temperature and impurity concentration, as the 1 mol% Fe-doped $Mg(OH)_2$ dehydrated at ~360°C and the others at ~320°C (Fig. S5 (A), (B)). In contrast, the Mn-doped $Mg(OH)_2$ all displayed similar dehydration temperatures of ~350°C (Fig. S5 (C), (D)).

3.2. Endmember $Mg(OH)_2$ Carbonation Reaction Sequence. At 1 bar CO_2 and 100% relative humidity, both the endmember and doped $Mg(OH)_2$ formed amorphous magnesium carbonate (AMC), which then crystallized to $Mg(CO_3)_2{\cdot}3H_2O$ (nesquehonite) (Fig. 3), a common product of $Mg(OH)_2$ carbonation at low temperatures (<50℃).[76–88,59,89]). After one day of reaction, the morphology of the initial $Mg(OH)_2$ was nearly preserved, but aggregation was evident (Fig. 3 (B)). After 1 week there was still abundant crystalline $Mg(OH)_2$ remaining, but a broad peak was observable in XRD patterns at 30° 2θ (Fig. 3 (E)), a characteristic feature of amorphous magnesium carbonate (AMC)[90]. The $Mg(OH)_2$ particles were aggregated at 1 week to the extent that particle boundaries are almost not observable (Fig. 3(C)).

After two weeks, some of the endmember $Mg(OH)_2$ had transformed to $Mg(CO_3)_2{\cdot}3H_2O$ (Fig. 3 (E)). Columnar $Mg(CO_3)_2{\cdot}3H_2O$ crystals (~3 μm length) were observed on the surface of the aggregated $Mg(OH)_2$ particles (Fig. 3 (D)). During the phase transformation, the BET surface

area decreased significantly from 56.6(3) m^2/g to 4.12(5) m^2/g – a 92 % decrease in surface area (Fig. S10). This surface area reduction likely originated from particle aggregation during AMC formation and the transformation to nesquehonite. As substantial $Mg(OH)_2$ was detected after 2 weeks of carbonation, the significant reduction in surface area suggests that the armoring observed during MgO carbonation[11] may also slow reaction rates. The phase evolution of the Fe- and Mn-doped $Mg(OH)_2$ was nearly identical to that of endmember $Mg(OH)_2$ (Table S8) during carbonation, but the reaction extent and kinetics varied.

3.3. Quantification of CO_2 Sorbence by Endmember and Doped $Mg(OH)_2$. As revealed by TGA-MS, the $Mg(OH)_2$ samples that were carbonated for two weeks experienced two major mass losses from 25-180℃ and 350-450℃ (Fig. S11, S12, S13). A small amount of CO_2 was detected in the nominally uncarbonated endmember $Mg(OH)_2$. This impurity likely originated from reaction of the NaOH solution with the atmospheric CO_2 during synthesis, but rapid reaction between the $Mg(OH)_2$ and atmospheric CO_2 is also a possible explanation. Because the NaOH solutions for the Fe- and Mn-doped $Mg(OH)_2$ were prepared in atmosphere, a small amount of CO_2 was also detected in the starting Fe- and Mn-doped $Mg(OH)_2$ (Fig. S12 (A), (B), (C) and S13 (A), (B), (C)). The first mass loss may represent adsorbed H_2O and CO_2 or decomposition of amorphous magnesium carbonate. The second may be from the decomposition of $Mg(OH)_2$, AMC, and/or nesquehonite.

The mass losses of the carbonated $Mg(OH)_2$ as a function of time indicate that: 1) reaction kinetics slowed significantly with time, and 2) Fe- and Mn-doped $Mg(OH)_2$ reacted more rapidly and to a greater extent than endmember $Mg(OH)_2$ (Fig. 4 (A), (B)). The variance of total mass loss as a function of impurity concentrations among the metal-doped $Mg(OH)_2$ was minimal, especially for Mn-doped $Mg(OH)_2$. The mass loss of Mn-doped $Mg(OH)_2$ showed little variance as a function

of Mn-concentration; it was largest for 3 mol% Mn (64 wt.%) and smallest for 5 mol% Mn (62 wt.%) after 2 weeks of carbonation. The effect of Fe-concentration on total mass loss was largest for 3 mol% Fe-doped $Mg(OH)_2$ (63 wt.%), followed by 5 mol% (61 wt.%), and 1 mol% (58 wt.%) Fe after 2 weeks of carbonation. It was challenging to quantify how much CO_2 was present in the volatiles because the temperature ranges over which CO_2 and H_2O evolve from the samples overlap, and the mass spectrometry signal is not a robust measure since the baseline is unclear. However, we suggest that the total weight loss can be a relative indicator for the amount of absorbed CO_2, based on the fact that 1) the sequences of phase transformation were the same for all samples (Table S8), and 2) the ratio of mass 18 to 44 (H_2O to CO_2) in the mass spectrometry signal did not vary significantly as a function of the dopant concentration (Table S9). These indicate that the reaction products are the same in each sample.

4. Discussion

4.1. Disposition of Fe and Mn Impurities in Doped $Mg(OH)_2$. We have considered several possibilities for the locations of the impurities: 1) The formation of either amorphous or crystalline secondary Fe-Mn (hydr)oxide phases; 2) Surface-sorption of Fe and Mn; 3) Intercalation of Fe and Mn in the $Mg(OH)_2$ interlayers; and 4) Fe and Mn substitution for octahedral Mg.

Neither our XRD nor TEM interrogations of the powders yielded evidence for secondary phases. Moreover, if the excess Fe formed a separate Fe (hydr)oxide phase, our magnetic susceptibility data showed that it must be non-magnetic at 2 K. Yet, most iron hydroxides and oxides are magnetic at low temperature[91], with the exception of green rust

389 ($[Fe_2^{3+}Fe^{2+}(OH)_6]^{2+}\cdot[(OH)_2]^{2-}$)[92]. Green rust, however, should have been detected with
390 synchrotron XRD[93], but was not. Similarly, synchrotron XRD ruled out a crystalline Mn secondary
391 phase, unless it was too poorly crystalline to be distinguished.

392 Although we cannot completely rule out the possibilities of some amount of surface
393 sorption or the existence of trace amorphous phases, we cite two observations that support the
394 disposition of Fe and Mn impurities through the replacement of octahedral Mg^{2+}: 1) Materials with
395 the brucite structure but with Fe and Mn in the octahedral sites do exist. Natural ferroan brucites
396 can contain a wide range of Fe(II)[50,51] concentrations. Endmember amakinite ($Fe(OH)_2$)[94] is highly
397 reactive at ambient conditions and rapidly oxidizes when exposed to the atmosphere[73]. Moreover,
398 researchers have analyzed synthetic ferrian brucites with up to ~15 mol% Fe(III) substitution in
399 the octahedral site[95]. Likewise, pyrochroite ($Mn(OH)_2$) occurs as a hydration product of
400 manganosite or rhodochrosite in hydrothermal environments[96,97], and phyllomanganates such as
401 feitknechtite ($Mn^{3+}OOH$)[98] with octahedral Mn(III) occur as natural minerals. 2) Our Rietveld
402 analyses of the doped Fe- and Mn- $Mg(OH)_2$ yielded occupancies that were in excellent agreement
403 with the values measured by ICP-OES. These refinements converged on the nominal
404 concentrations both when the starting Fe- and Mn-occupancies were higher or lower than the
405 nominal values, indicating a high robustness for the result.

406 **4.2. Oxidation States of Fe and Mn.** Our *ab initio* molecular dynamical simulations
407 suggested that the substitution of Fe^{2+} or Mn^{2+} for Mg^{2+}in $Mg(OH)_2$ is viable but not energetically
408 favorable. The substitution energies are shown in Table S7. The incorporation of one Fe^{2+} per 32
409 cations (~3.2 mol% Fe^{2+}) into $Mg(OH)_2$ showed a marginal increase in ΔE of 0.1 eV. Incorporation
410 of two Fe^{2+} per 32 cations (~6.4 mol% Fe^{2+}) increased the substitution energy to 2.0 eV. The
411 energy for incorporation of one Mn^{2+} per 32 cations (~3.2 mol% Mn^{2+}) was significantly higher

412 (6.3 eV) than that of Fe^{2+}. An increase in entropy may compensate for these higher energies to
413 some extent, but the substitutions, especially of Mn^{2+}, are still likely to be energetically
414 unfavorable. In addition, our modeled incorporation of divalent Fe or Mn into $Mg(OH)_2$ did not
415 suggest a change in the oxidation states of the metal ions. The Mulliken charges and spin states of
416 both Fe and Mn were similar to that of the hydrated divalent metal ion in water.

417 We did not, however, simulate the substitution of trivalent Fe and Mn for Mg^{2+}. Since our
418 Mössbauer spectroscopy and magnetometry showed conclusively that substitution of Mg by Fe
419 was accompanied by Fe oxidation, energy calculations that presume constancy in redox states may
420 yield misleading predictions. Neither Mössbauer nor magnetometry data will reveal oxidation
421 states for substituted Mn, but color changes in our doped $Mg(OH)_2$ are highly suggestive. Just as
422 Fe-doped $Mg(OH)_2$ transitioned from light blue to light yellow (1 mol% Fe) to orange (5 mol%
423 Fe) in ~10 hours, we observed Mn-doped $Mg(OH)_2$ change from pink to light blue (1 mol% Mn)
424 to dark pink (5 mol% Mn) (Fig. S8). Endmember pyrochroite likewise oxidizes spontaneously at
425 ambient conditions, and we speculate that our Mn-doped $Mg(OH)_2$ contained some fraction of
426 Mn(III) and/or Mn(IV).

427 If trivalent or tetravalent impurities substitute for Mg^{2+}, the extra charge should be
428 compensated either by Mg^{2+} vacancies, by interlayer anions such as Cl^-, or by deprotonation of the
429 Mg-trioctahedral sheets[95]. The small differences in c ($\leq$ 0.016(1) Å) between endmember
430 $Mg(OH)_2$ and doped $Mg(OH)_2$ may rule out the possibility of charge compensation by interlayer
431 anions. Deprotonation should shorten the bond length between the impurity cations and oxygen.
432 Moreover, the smaller radii of Fe(III) and Mn(III) and Mn(IV) relative to Mg^{2+} will also decrease
433 the metal-oxygen bond lengths (Fe(II): 0.92 Å; Fe(III): 0.785 Å; Mn(II): 0.97 Å; Mn(III): 0.785
434 Å; Mn(IV): 0.67 Å; Mg^{2+}: 0.86 Å)[99].

435 Our Rietveld refinements yielded metal-oxygen bond distances that were consistent with
436 the substitution of Fe and Mn in our inferred oxidation states (Table S1). Our refined Mg-O bond
437 length for endmember $Mg(OH)_2$ was 2.0819(8) Å, in good agreement with 2.099 Å from the
438 single-crystal refinement of Zigan et al. [100]. Our Rietveld analysis of Fe-doped $Mg(OH)_2$ yielded
439 M-O bond lengths of 2.062(2) Å (3 mol%) and 2.048(2) Å (5 mol%), shorter than those observed
440 in endmember $Mg(OH)_2$, as would be expected if Fe(III) were replacing Mg^{2+}. The disparity in M-
441 O bond lengths between endmember $Mg(OH)_2$ and Mn-doped $Mg(OH)_2$ was present but less
442 significant, as might be expected if concentrations of Mn(III) or Mn(IV) were lower than in the Fe
443 system. Therefore, we suggest that Fe and Mn substituted for Mg^{2+}, accompanied by deprotonation
444 from the octahedral sheets.

445 **4.3. Effect of Iron and Manganese Doping on the Carbonation Efficiency of $Mg(OH)_2$.**

446 The total mass loss of endmember and Fe- and Mn-doped $Mg(OH)_2$ at 700°C (Fig. 4 (A),
447 (B)) indicates that the Fe- and Mn-doped $Mg(OH)_2$ (maximum reactivity at 3 mol%) were slightly
448 better sorbents of CO_2 in terms of both kinetics and reaction extent than endmember $Mg(OH)_2$,
449 possibly due to their higher initial surface areas. Alternatively, the lower temperatures at which
450 the Fe- and Mn-doped $Mg(OH)_2$ broke down during TGA-MS analysis indicates that they are less
451 stable than endmember $Mg(OH)_2$. In addition, the XRD of Fe- and Mn-doped $Mg(OH)_2$ showed
452 broader *c*-component peaks and larger *c* dimensions than the endmember material. These
453 observations suggest that Fe and Mn doping may cause stacking faults along the *c*-direction that
454 increase its reactivity. Vessey et al. (2024)[59] observed that carbonation of high Fe-doped brucite
455 led to the formation of secondary amorphous phases that inhibited CDR. Our results suggest that
456 for Fe and Mn impurity concentrations up to 5 mol%, inhibition by secondary amorphous phases
457 is superseded by the effects of grain size and stacking defects, which favor CDR.

A doping concentration of 3 mol% induced the maximum reactivity for both Fe- and Mn-substituted $Mg(OH)_2$. Higher concentrations (5 mol%) decreased reactivity. Although this reversal may be explained by differences in the surface areas among the Mn-doped $Mg(OH)_2$, it cannot account for the behaviors of the Fe-doped $Mg(OH)_2$, because the surface area of the 5 mol% Fe-doped $Mg(OH)_2$ was slightly higher than that of the 3 mol% Fe-doped $Mg(OH)_2$ (Table S6). We caution against overinterpreting these results, however, since there is only a single synthesis for each composition, and some undetermined phenomenon could be affecting the individual ranking of the reaction extents as a function of dopant concentration and composition. Regardless, this composition dependence is consistent with Vessey et al. (2024)[59], who observed decreasing carbonation efficiency with increasing Fe content from 6 to 44%, all higher than our highest iron concentration (5 mol%). Future work might focus on a more robust quantification of the reaction kinetics, building on the understanding of the mechanisms by which the impurities act determined here.

5. Conclusions

Brucite can be synthesized or extracted from both natural and industrial sources, and it often includes metal impurities such as Fe or Mn. Our combined experimental and computational results show that Fe- and Mn-doped $Mg(OH)_2$ with impurity concentrations up to 5 mol% are better sorbent candidates than endmember $Mg(OH)_2$. Up to 5 mol% of Fe and Mn increases the carbonation reaction extent due to increased surface area and lower stability. These results suggest that the doped material will capture more CO_2, more rapidly than endmember $Mg(OH)_2$. Regardless of the extent of metal doping, however, TGA-MS weight loss of the carbonated phase

480 during heating occurred in two steps, the first at 25-180℃ and the second at 350-450℃, following
481 a phase evolution sequence containing an amorphous intermediate: $Mg(OH)_2$ (brucite) →
482 $MgCO_3 \cdot nH_2O$ (AMC) → $MgCO_3 \cdot 3H_2O$ (nesquehonite). However, the reactivities of Fe- and Mn-
483 doped $Mg(OH)_2$ varied with the concentration and impurity. Fe $Mg(OH)_2$ with 3 mol% doping
484 showed the highest reactivity followed by 5 mol% and 1 mol% Fe doping. Mn-doped $Mg(OH)_2$
485 similarly was optimized at 3 mol% substitution, followed by 1 mol% and 5 mol% Mn $Mg(OH)_2$.
486 Therefore, although future long-term carbonation experiments at the ambient CO_2 pressure and
487 humidity are need for validation, we suggest that natural or industrial waste $Mg(OH)_2$ with Fe and
488 Mn impurities may be targeted as superior CDR sorbents than endmember $Mg(OH)_2$ when their
489 impurity concentrations fall below 5 mol%.
490

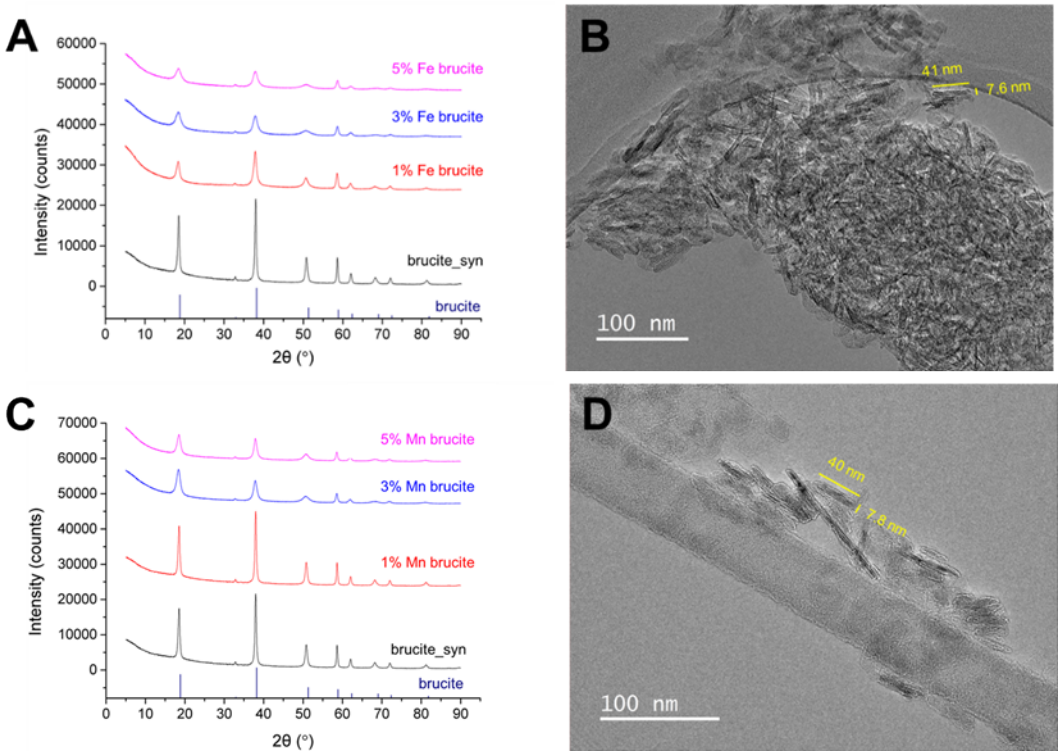

Figure 1: Characterization of synthetic Fe- and Mn-doped $Mg(OH)_2$. (A) XRD patterns of Fe-doped $Mg(OH)_2$: 1 mol% (red), 3 mol% (blue), and 5 mol% (magenta) Fe-doped $Mg(OH)_2$ with endmember $Mg(OH)_2$ (black) as a reference. (B) Representative TEM image of 1 mol% Fe $Mg(OH)_2$. (C) XRD pattern of Mn-doped $Mg(OH)_2$: 1 mol% (red), 3 mol% (blue), and 5 mol% (magenta) Mn-doped $Mg(OH)_2$ with endmember $Mg(OH)_2$ (black) as a reference. (D) Representative TEM image of 1 mol% Mn-doped $Mg(OH)_2$.

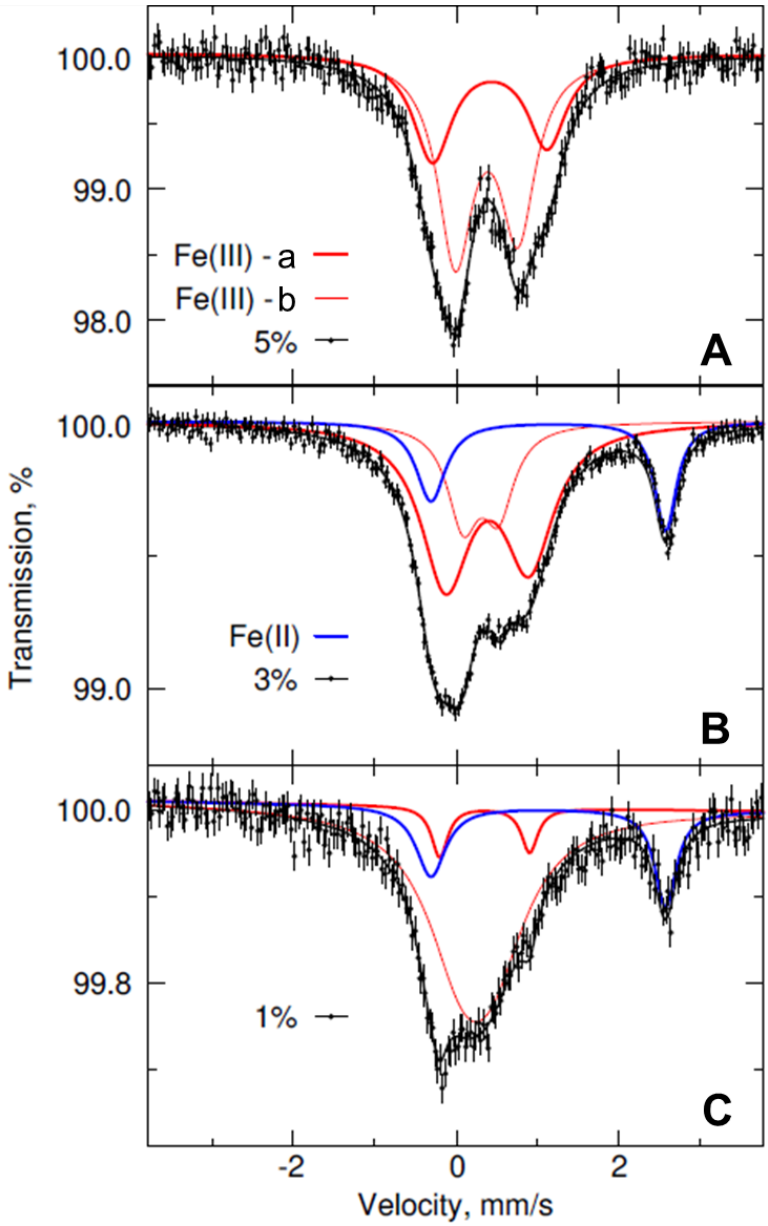

Figure 2: Mössbauer characterization of Fe-doped $Mg(OH)_2$ with fitting curves: (A) 5 mol%, (B) 3 mol%, (C) 1 mol% Fe-doped $Mg(OH)_2$. Note that 5 mol% Fe-doped $Mg(OH)_2$ contains only Fe (III) but 1 mol% and 3 mol% Fe-doped $Mg(OH)_2$ contain some Fe(II) as well as Fe(III).

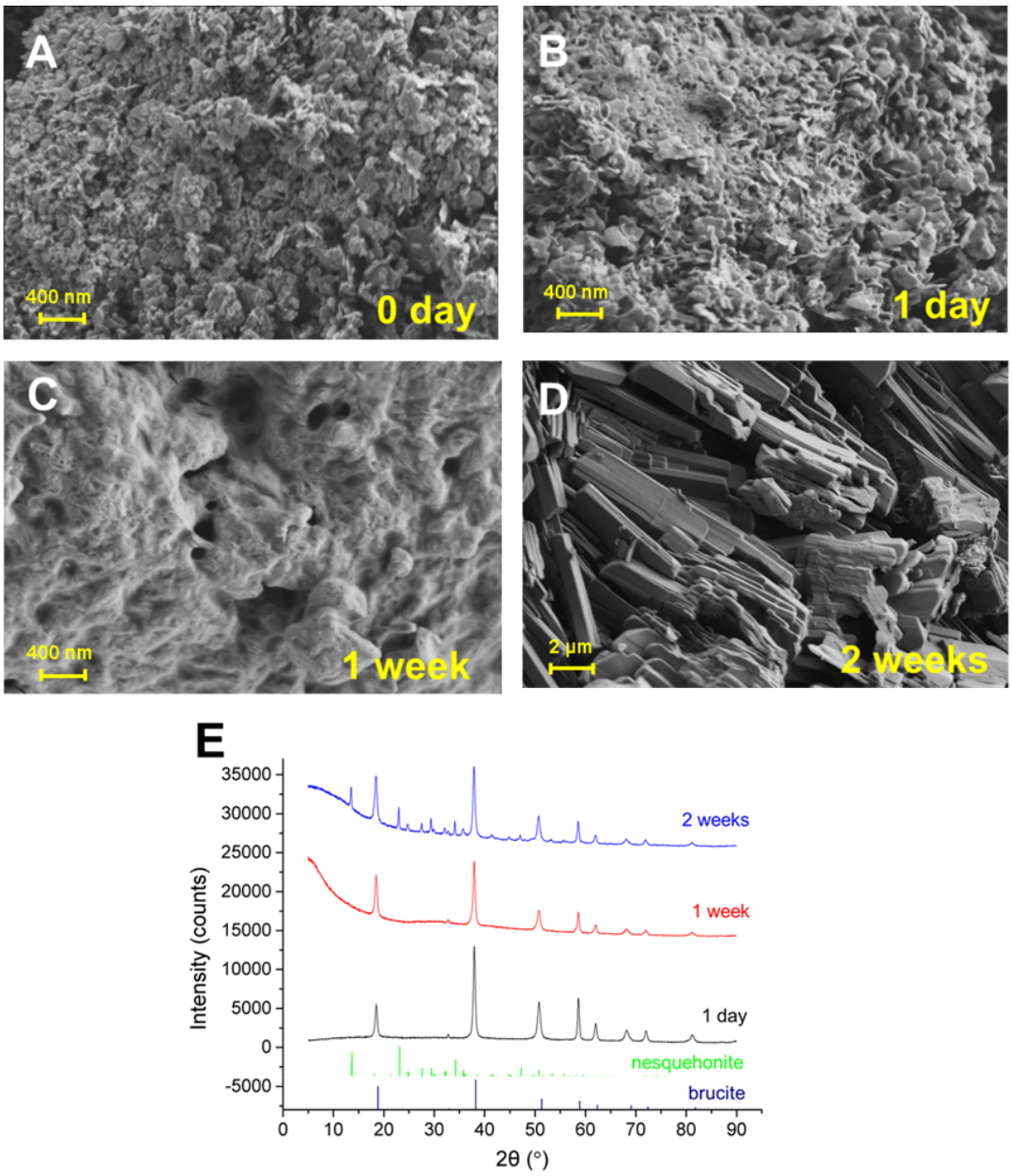

Figure 3: Evolution of endmember $Mg(OH)_2$ during carbonation as a function of the carbonation time. SEM image of (A) starting endmember $Mg(OH)_2$, after carbonation for (B) 1 day, (C) 1 week, and (D) 2 weeks. (E) The XRD pattern of endmember $Mg(OH)_2$ as a function of carbonation time. Refer to Figure 1 (A) and (C) for the XRD pattern of starting endmember $Mg(OH)_2$[101,102].

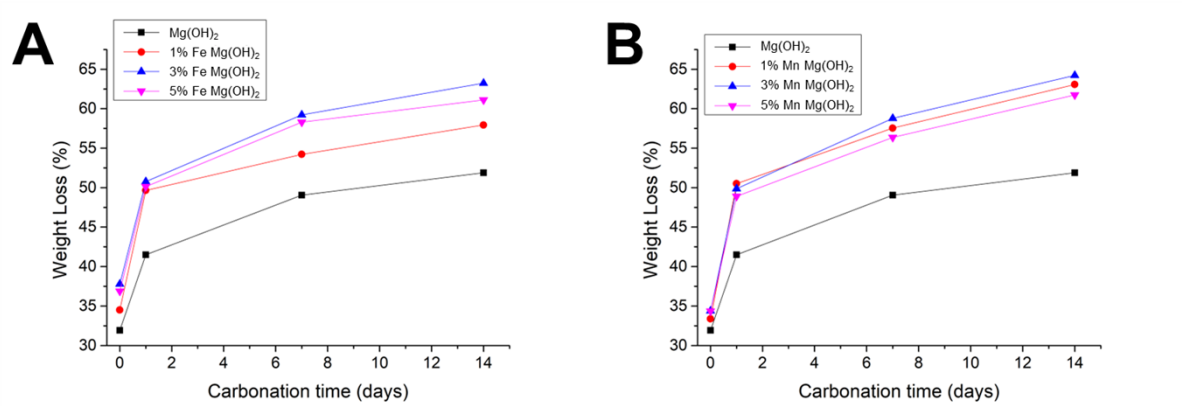

Figure 4: The total weight loss at 700°C of (A) Fe- and (B) Mn-doped $Mg(OH)_2$ as a function of carbonation time: 1 mol% (red), 3 mol% (blue), and 5 mol% (magenta) Fe- or Mn-doped $Mg(OH)_2$ with endmember $Mg(OH)_2$ (black) as a reference.

496

497

Acknowledgments

This article is based on Chapter 3 of Dong Youn Chung`s PhD thesis[103]. This work was mainly supported by the U.S. Department of Energy (DOE), Office of Science, Basic Energy Sciences (BES), Materials Sciences and Engineering Division. TEM and SEM characterization was conducted as part of a user project at the Center for Nanophase Materials Sciences (CNMS), which is a U.S. Department of Energy, Office of Science User Facility at Oak Ridge National Laboratory. The synchrotron XRD measurements were performed at GeoSoilEnviroCARS (The University of Chicago, Sector 13), Advanced Photon Source (APS), Argonne National Laboratory (ANL). GeoSoilEnviroCARS was supported by the National Science Foundation – Earth Sciences (EAR – 1634415). This research used resources of the APS, a U.S. Department of Energy (DOE) Office of Science User Facility operated for the DOE Office of Science by ANL under Contract No. DE-AC02-06CH11357. Synchrotron-XRD measurements were funded by U.S. National Science Foundation (NSF) grant EAR-1925903, American Chemical Society Petroleum Research Fund (ACS PRF), and the Pennsylvania State University.

Supporting Information

Additional experimental details, methods including a figure of the experimental setup, and results: Mössbauer spectrum, magnetization, ab initio MD simulation, synchrotron XRD, SEM images, TGA-MS, BET surface area, Rietveld refinement, ICP-OES, and phase evolution of brucites.

519 References

520 (1) Lackner, K. S.; Wendt, C. H.; Butt, D. P.; Joyce Jr, E. L.; Sharp, D. H. Carbon Dioxide
521 Disposal in Carbonate Minerals. *Energy* **1995**, *20* (11), 1153–1170.

522 (2) Lackner, K. S.; Butt, D. P.; Wendt, C. H. Progress on Binding CO_2 in Mineral Substrates.
523 *Energy Conversion and Management* **1997**, *38*, S259–S264.

524 (3) Blamey, J.; Anthony, E. J.; Wang, J.; Fennell, P. S. The Calcium Looping Cycle for Large-
525 Scale CO_2 Capture. *Progress in Energy and Combustion Science* **2010**, *36* (2), 260–279.

526 (4) Hosseinpour, M.; Hejazi, B.; Criado, Y. A. Techno-Economic Study of a Direct Air Capture
527 System Based on the Carbonation of $Ca(OH)_2$ Plates Integrated into Cooling Towers. *Journal*
528 *of Cleaner Production* **2025**, *486*, 144545.

529 (5) Dostie, L.; Power, I. M.; Rausis, K. Carbon Dioxide Supply and Scaling Constraints on Direct
530 Air Capture Using Calcium Oxide Powder. *Journal of Cleaner Production* **2025**, *527*,
531 146635.

532 (6) Wang, E.; Navik, R.; Miao, Y.; Gao, Q.; Izikowitz, D.; Chen, L.; Li, J. Reviewing Direct Air
533 Capture Startups and Emerging Technologies. *Cell Reports Physical Science* **2024**, *5* (2).

534 (7) McQueen, N.; Gomes, K. V.; McCormick, C.; Blumanthal, K.; Pisciotta, M.; Wilcox, J. A
535 Review of Direct Air Capture (DAC): Scaling up Commercial Technologies and Innovating
536 for the Future. *Progress in Energy* **2021**, *3* (3), 032001.

537 (8) Olajire, A. A. A Review of Mineral Carbonation Technology in Sequestration of CO_2.
538 *Journal of Petroleum Science and Engineering* **2013**, *109*, 364–392.

(9) Alper, E.; Orhan, O. Y. CO_2 Utilization: Developments in Conversion Processes. *Petroleum* **2017**, *3* (1), 109–126.

(10) McQueen, N.; Kelemen, P.; Dipple, G.; Renforth, P.; Wilcox, J. Ambient Weathering of Magnesium Oxide for CO_2 Removal from Air. *Nat. Commun.* **2020**, *11* (1), 1.

(11) Weber, J.; Starchenko, V.; Yuan, K.; Anovitz, L. M.; Ievlev, A. V.; Unocic, R. R.; Borisevich, A. Y.; Boebinger, M. G.; Stack, A. G. Armoring of MgO by a Passivation Layer Impedes Direct Air Capture of CO_2. *Environ. Sci. Technol.* **2023**, *57* (40), 14929–14937. https://doi.org/10.1021/acs.est.3c04690.

(12) Grasa, G. S.; Abanades, J. C. CO_2 Capture Capacity of CaO in Long Series of Carbonation/Calcination Cycles. *Ind. Eng. Chem. Res.* **2006**, *45* (26), 8846–8851. https://doi.org/10.1021/ie0606946.

(13) Song, G.; Ding, Y.-D.; Zhu, X.; Liao, Q. Carbon Dioxide Adsorption Characteristics of Synthesized MgO with Various Porous Structures Achieved by Varying Calcination Temperature. *Colloids and Surfaces A: Physicochemical and Engineering Aspects* **2015**, *470*, 39–45.

(14) Patel, A. S.; Raudsepp, M. J.; Wilson, S.; Harrison, A. L. Water Activity Controls the Stability of Amorphous Ca–Mg-and Mg-Carbonates. *Crystal Growth & Design* **2024**, *24* (5), 2000–2013.

(15) Ding, W.; Ouyang, J.; Yang, H. Synthesis and Characterization of Nesquehonite ($MgCO_3 \cdot 3H_2O$) Powders from Natural Talc. *Powder Technology* **2016**, *292*, 169–175. https://doi.org/10.1016/j.powtec.2016.01.037.

(16) Hu, C.; Liu, Y.; Qian, X.; Qin, Y.; Dong, Y.; Wang, F. Energy-Saving Calcination of Hydromagnesite for Sustainable Magnesia-Based Cement: A New Route towards MgO Production. *Construction and Building Materials* **2024**, *419*, 135593. https://doi.org/10.1016/j.conbuildmat.2024.135593.

(17) Yamamoto, G.; Kyono, A.; Okada, S. Thermal Decomposition Process of Dypingite $Mg_5(CO_3)_4(OH)_2 \cdot 5H_2O$. *Materials Letters* **2022**, *308*, 131125. https://doi.org/10.1016/j.matlet.2021.131125.

(18) Li, P.; Liu, W.; Dennis, J. S.; Zeng, H. C. Synthetic Architecture of MgO/C Nanocomposite from Hierarchical-Structured Coordination Polymer toward Enhanced CO_2 Capture. *ACS Appl. Mater. Interfaces* **2017**, *9* (11), 9592–9602. https://doi.org/10.1021/acsami.6b14960.

(19) Jin, S.; Ko, K.-J.; Lee, C.-H. Direct Formation of Hierarchically Porous MgO-Based Sorbent Bead for Enhanced CO_2 Capture at Intermediate Temperatures. *Chemical Engineering Journal* **2019**, *371*, 64–77.

(20) Pang, H.; Sun, A.; Xu, H.; Xiao, G. Regenerable MgO-Based Sorbents for CO_2 Capture at Elevated Temperature and Pressure: Experimental and DFT Study. *Chemical Engineering Journal* **2021**, *425*, 130675.

(21) Sandalow, D.; Aines, R.; Friedmann, J.; Kelemen, P.; McCormick, C.; Power, I.; Schmidt, B.; Wilson, S. *Carbon Mineralization Roadmap Draft October 2021*; Lawrence Livermore National Lab.(LLNL), Livermore, CA (United States), 2021.

(22) Boschi, C.; Dini, A.; Baneschi, I.; Bedini, F.; Perchiazzi, N.; Cavallo, A. Brucite-Driven CO_2 Uptake in Serpentinized Dunites (Ligurian Ophiolites, Montecastelli, Tuscany). *Lithos* **2017**, *288*, 264–281.

(23) Cook, S. J.; Bowman, J. R. Contact Metamorphism Surrounding the Alta Stock: Thermal Constraints and Evidence of Advective Heat Transport from Calcite + Dolomite Geothermometry. *American Mineralogist* **1994**, *79* (5–6), 513–525.

(24) Mohamed, A.-M. O.; El Gamal, M.; Hameedi, S. M.; Paleologos, E. K. Chapter 12 - Carbonation of Mine Tailings Waste. In *Sustainable Utilization of Carbon Dioxide in Waste Management*; Mohamed, A.-M. O., El Gamal, M., Hameedi, S. M., Paleologos, E. K., Eds.; Elsevier, 2023; pp 449–493. https://doi.org/10.1016/B978-0-12-823418-1.00012-3.

(25) Chrysochoou, M.; Dermatas, D.; Grubb, D. G.; Moon, D. H.; Christodoulatos, C. Importance of Mineralogy in the Geoenvironmental Characterization and Treatment of Chromite Ore Processing Residue. *J. Geotech. Geoenviron. Eng.* **2010**, *136* (3), 510–521. https://doi.org/10.1061/(ASCE)GT.1943-5606.0000233.

(26) Pronost, J.; Beaudoin, G.; Tremblay, J.; Larachi, F.; Duchesne, J.; Hébert, R.; Constantin, M. Carbon Sequestration Kinetic and Storage Capacity of Ultramafic Mining Waste. *Environ. Sci. Technol.* **2011**, *45* (21), 9413–9420. https://doi.org/10.1021/es203063a.

(27) Power, I. M.; Harrison, A. L.; Dipple, G. M.; Wilson, S.; Kelemen, P. B.; Hitch, M.; Southam, G. Carbon Mineralization: From Natural Analogues to Engineered Systems. *Reviews in Mineralogy and Geochemistry* **2013**, *77* (1), 305–360.

(28) Renforth, P. The Negative Emission Potential of Alkaline Materials. *Nature communications* **2019**, *10* (1), 1401.

(29) Cipollina, A.; Bevacqua, M.; Dolcimascolo, P.; Tamburini, A.; Brucato, A.; Glade, H.; Buether, L.; Micale, G. Reactive Crystallisation Process for Magnesium Recovery from Concentrated Brines. *Desalination and Water Treatment* **2015**, *55* (9), 2377–2388. https://doi.org/10.1080/19443994.2014.947771.

(30) Romano, S.; Trespi, S.; Achermann, R.; Battaglia, G.; Raponi, A.; Marchisio, D.; Mazzotti, M.; Micale, G.; Cipollina, A. The Role of Operating Conditions in the Precipitation of Magnesium Hydroxide Hexagonal Platelets Using NaOH Solutions. *Crystal Growth & Design* **2023**, *23* (9), 6491–6505. https://doi.org/10.1021/acs.cgd.3c00462.

(31) Battaglia, G.; Ventimiglia, L.; Vicari, F.; Tamburini, A.; Cipollina, A.; Micale, G. Characterization of $Mg(OH)_2$ Powders Produced from Real Saltworks Bitterns at a Pilot Scale. *Powder Technology* **2024**, *443*, 119918. https://doi.org/10.1016/j.powtec.2024.119918.

(32) Caceres, P. G.; Attiogbe, E. K. Thermal Decomposition of Dolomite and the Extraction of Its Constituents. *Minerals Engineering* **1997**, *10* (10), 1165–1176.

(33) Bernard, E.; Nguyen, H.; Kawashima, S.; Lothenbach, B.; Manzano, H.; Provis, J.; Scott, A.; Unluer, C.; Winnefeld, F.; Kinnunen, P. MgO-Based Cements–Current Status and Opportunities. *RILEM Technical Letters* **2023**, *8*, 65–78.

(34) Dunstan, M. T.; Donat, F.; Bork, A. H.; Grey, C. P.; Müller, C. R. CO_2 Capture at Medium to High Temperature Using Solid Oxide-Based Sorbents: Fundamental Aspects, Mechanistic Insights, and Recent Advances. *Chemical reviews* **2021**, *121* (20), 12681–12745.

(35) Gao, W.; Zhou, T.; Wang, Q. Controlled Synthesis of MgO with Diverse Basic Sites and Its CO_2 Capture Mechanism under Different Adsorption Conditions. *Chemical Engineering Journal* **2018**, *336*, 710–720.

(36) Han, K. K.; Zhou, Y.; Chun, Y.; Zhu, J. H. Efficient MgO-Based Mesoporous CO_2 Trapper and Its Performance at High Temperature. *Journal of hazardous materials* **2012**, *203*, 341–347.

(37) Han, K. K.; Zhou, Y.; Lin, W. G.; Zhu, J. H. One-Pot Synthesis of Foam-like Magnesia and Its Performance in CO_2 Adsorption. *Microporous and mesoporous materials* **2013**, *169*, 112–119.

(38) Thomele, D.; Bourret, G. R.; Bernardi, J.; Bockstedte, M.; Diwald, O. Hydroxylation Induced Alignment of Metal Oxide Nanocubes. *Angewandte Chemie International Edition* **2017**, *56* (5), 1407–1410.

(39) Zheng, X.; Cordonnier, B.; McBeck, J.; Boller, E.; Jamtveit, B.; Zhu, W.; Renard, F. Mixed-Mode Strain Localization Generated by Hydration Reaction at Crustal Conditions. *JGR Solid Earth* **2019**, *124* (5), 4507–4522. https://doi.org/10.1029/2018JB017008.

(40) Tajuelo Rodriguez, E.; Anovitz, L. M.; Adapa, S.; Yuan, K.; Hensley, D.; Chung, D. Y.; Boebinger, M. G.; Stack, A. G.; Weber, J. Effect of Multiple Calcination Cycles on CO_2

638 Capture Efficiency during Carbonation of MgO in a Mineral Looping Process. *Scientific*
639 *Reports* **2025**, *15* (1), 39193.

640 (41) Stumm, W.; Morgan, J. J. *Aquatic Chemistry: Chemical Equilibria and Rates in Natural*
641 *Waters*; John Wiley & Sons, 2013.

642 (42) Stack, A. G. Next Generation Models of Carbonate Mineral Growth and Dissolution:
643 Modeling and Analysis: Next Generation Models of Carbonate Mineral Growth and
644 Dissolution. *Greenhouse Gas Sci Technol* **2014**, *4* (3), 278–288.
645 https://doi.org/10.1002/ghg.1400.

646 (43) Røyne, A.; Jamtveit, B. Pore-Scale Controls on Reaction-Driven Fracturing. *Reviews in*
647 *Mineralogy and Geochemistry* **2015**, *80* (1), 25–44.

648 (44) Kuleci, H.; Schmidt, C.; Rybacki, E.; Petrishcheva, E.; Abart, R. Hydration of Periclase at
649 350 °C to 620 °C and 200 MPa: Experimental Calibration of Reaction Rate. *Mineralogy and*
650 *Petrology* **2016**, *110*, 1–10.

651 (45) Luong, N. T.; Boily, J.-F. Water Film-Driven Brucite Nanosheet Growth and Stacking.
652 *Langmuir* **2023**, *39* (31), 11090–11098. https://doi.org/10.1021/acs.langmuir.3c01411.

653 (46) Dostie, L.; Rausis, K.; Power, I. M. Passive Direct Air Capture Using Calcium Oxide Powder:
654 The Importance of Water Vapor. *Journal of Cleaner Production* **2024**, *457*, 142394.
655 https://doi.org/10.1016/j.jclepro.2024.142394.

656 (47) Bracco, J. N.; Camacho Meneses, G.; Colón, O.; Yuan, K.; Stubbs, J. E.; Eng, P. J.; Wanhala,
657 A. K.; Einkauf, J. D.; Boebinger, M. G.; Stack, A. G.; Weber, J. Reaction Layer Formation

on MgO in the Presence of Humidity. *ACS Appl. Mater. Interfaces* **2024**, *16* (1), 712–722. https://doi.org/10.1021/acsami.3c14823.

(48) Mumpton, F.; Jaffe, H. W.; Thompson, C. Coalingite, a New Mineral from the New Idria Serpentinite, Fresno and San Benito Counties, California. *American Mineralogist: Journal of Earth and Planetary Materials* **1965**, *50* (11–12), 1893–1913.

(49) Mumpton, F.; Thompson, C. The Stability of Brucite in the Weathering Zone of the New Idria Serpentinite. In *Clays and Clay Minerals*; Elsevier, 1966; pp 249–257.

(50) Templeton, A. S.; Ellison, E. T. Formation and Loss of Metastable Brucite: Does Fe(II)-Bearing Brucite Support Microbial Activity in Serpentinizing Ecosystems? *Philosophical Transactions of the Royal Society A: Mathematical, Physical and Engineering Sciences* **2020**, *378* (2165), 20180423. https://doi.org/10.1098/rsta.2018.0423.

(51) Beard, J. S.; Hopkinson, L. A Fossil, Serpentinization-related Hydrothermal Vent, Ocean Drilling Program Leg 173, Site 1068 (Iberia Abyssal Plain): Some Aspects of Mineral and Fluid Chemistry. *Journal of Geophysical Research: Solid Earth* **2000**, *105* (B7), 16527–16539.

(52) Bowles, J. F. W. Hydroxides. In *Encyclopedia of Geology (Second Edition)*; Alderton, D., Elias, S. A., Eds.; Academic Press: Oxford, 2021; pp 442–451. https://doi.org/10.1016/B978-0-08-102908-4.00162-4.

(53) Dias, A. S.; Barriga, F. J. Mineralogy and Geochemistry of Hydrothermal Sediments from the Serpentinite-Hosted Saldanha Hydrothermal Field (36 34′ N; 33 26′ W) at MAR. *Marine Geology* **2006**, *225* (1–4), 157–175.

(54) Holtstam, D.; Langhof, J. *Långban: The Mines, Their Minerals, Geology and Explorers*; Raster Förlag, 1999.

(55) Palache, C.; Berman, H.; Frondel, C. Dana's System of Mineralogy. *Geologiska Föreningen i Stockholm Förhandlingar* **1952**, *74* (2), 218–219.

(56) Wright, K.; Cygan, R. T.; Slater, B. Impurities and Nonstoichiometry in the Bulk and on the (10$\bar{1}$4) Surface of Dolomite. *Geochimica et Cosmochimica Acta* **2002**, *66* (14), 2541–2546. https://doi.org/10.1016/S0016-7037(02)00846-3.

(57) Casas, S.; Aladjem, C.; Larrotcha, E.; Gibert, O.; Valderrama, C.; Cortina, J. L. Valorisation of Ca and Mg By-products from Mining and Seawater Desalination Brines for Water Treatment Applications. *J of Chemical Tech & Biotech* **2014**, *89* (6), 872–883. https://doi.org/10.1002/jctb.4326.

(58) Alegbe, M. J.; Ayanda, O. S.; Ndungu, P.; Fatoba, O. O.; Nechaev, A.; Petrik, L. F. Assessment of the Physical and Chemical Qualities of Brine and the Application of Nano Zerovalent Iron for the Treatment of Brine Effluent. *Desalination and Water Treatment* **2018**, *102*, 141–150.

(59) Vessey, C. J.; Raudsepp, M. J.; Patel, A. S.; Wilson, S.; Harrison, A. L.; Chen, N.; Chen, W. Influence of Iron Substitution and Solution Composition on Brucite Carbonation. *Environ. Sci. Technol.* **2024**, *58* (18), 7802–7813. https://doi.org/10.1021/acs.est.3c08708.

(60) Zhao, S.; Zhao, Y.; Wu, Z.; Lv, F.; Lv, G. Evolution Process of Ferroan Brucite under Humid Conditions with CO_2 and O_2. *J. Phys. Chem. C* **2023**, *127* (33), 16395–16404. https://doi.org/10.1021/acs.jpcc.3c03422.

(61) Weber, J.; Moseley, B.; Yuan, K.; Evans, B. R.; Starchenko, V.; Tajuelo Rodriguez, E.; Chung, D. Y.; Boebinger, M. G.; McGuire, M. A.; Yumnam, G.; Hermann, R. P.; Anovitz, L. M.; Stack, A. G. Influence of Dissolved Iron in Solution on MgO Hydroxylation and Carbonation. *J. Phys. Chem. C* **2025**, *129* (1), 194–204. https://doi.org/10.1021/acs.jpcc.4c04953.

(62) Hadia, N. M. A.; Mohamed, H. A.-H. Characteristics and Optical Properties of MgO Nanowires Synthesized by Solvothermal Method. *Materials Science in Semiconductor Processing* **2015**, *29*, 238–244.

(63) Rietveld, H. M. A Profile Refinement Method for Nuclear and Magnetic Structures. *J Appl Cryst* **1969**, *2* (2), 65–71. https://doi.org/10.1107/S0021889869006558.

(64) Toby, B. H.; Von Dreele, R. B. GSAS-II: The Genesis of a Modern Open-Source All Purpose Crystallography Software Package. *Journal of Applied Crystallography* **2013**, *46* (2), 544–549.

(65) Brunauer, S.; Emmett, P. H.; Teller, E. Adsorption of Gases in Multimolecular Layers. *J. Am. Chem. Soc.* **1938**, *60* (2), 309–319. https://doi.org/10.1021/ja01269a023.

(66) Perdew, J. P. K. Burke, m. Ernzerhof. *Phys. Rev. Lett* **1996**, *77*, 3865.

(67) Anovitz, L. M.; Elam, J. M.; Riciputi, L. R.; Cole, D. R. Isothermal Time-Series Determination of the Rate of Diffusion of Water in Pachuca Obsidian. *Archaeometry* **2004**, *46* (2), 301–326. https://doi.org/10.1111/j.1475-4754.2004.00159.x.

(68) Rausis, K.; Stubbs, A. R.; Power, I. M.; Paulo, C. Rates of Atmospheric CO_2 Capture Using Magnesium Oxide Powder. *International Journal of Greenhouse Gas Control* **2022**, *119*, 103701.

(69) Brindley, G. W. Quantitative X-Ray Mineral Analysis of Clays. **1980**.

(70) Jeans, C. V. MOORE, DM & REYNOLDS, RC, Jr. 1997. X-Ray Diffraction and the Identification and Analysis of Clay Minerals, Xviii+ 378 Pp. Oxford, New York: Oxford University Press. Price\pounds 27.95 (Spiral-Bound Paperback). ISBN 0 19 508713 5. *Geological Magazine* **1998**, *135* (6), 819–842.

(71) Lourenço, M. P.; De Oliveira, C.; Oliveira, A. F.; Guimarães, L.; Duarte, H. A. Structural, Electronic, and Mechanical Properties of Single-Walled Chrysotile Nanotube Models. *J. Phys. Chem. C* **2012**, *116* (17), 9405–9411. https://doi.org/10.1021/jp301048p.

(72) Yuan, P.; Tan, D.; Annabi-Bergaya, F. Properties and Applications of Halloysite Nanotubes: Recent Research Advances and Future Prospects. *Applied Clay Science* **2015**, *112*, 75–93.

(73) Parise, J. B.; Marshall, W. G.; Smith, R. I.; Lutz, H. D.; Möller, H. The Nuclear and Magnetic Structure of "White Rust"—Fe $(OH_{0.86}D_{0.14})_2$. *American Mineralogist* **2000**, *85* (1), 189–193.

(74) Binfu, X.; Yilong, C. Mossbauer Study of Brucite (Mg, Fe)$(OH)_2$. *Wuhan Univ. J. Nat. Sci.* **1999**, *4* (1), 54–56. https://doi.org/10.1007/BF02827620.

(75) Blaauw, C.; Stroink, G.; Leiper, W.; Zentilli, M. Crystal-field Properties of Fe in Brucite $Mg(OH)_2$. *Physica Status Solidi (b)* **1979**, *92* (2), 639–643. https://doi.org/10.1002/pssb.2220920238.

(76) Zhao, L.; Sang, L.; Chen, J.; Ji, J.; Teng, H. H. Aqueous Carbonation of Natural Brucite: Relevance to CO_2 Sequestration. *Environ. Sci. Technol.* **2010**, *44* (1), 406–411. https://doi.org/10.1021/es9017656.

(77) Schaef, H. T.; Windisch Jr, C. F.; McGrail, B. P.; Martin, P. F.; Rosso, K. M. Brucite [Mg (OH_2)] Carbonation in Wet Supercritical CO_2: An in Situ High Pressure X-Ray Diffraction Study. *Geochimica et Cosmochimica Acta* **2011**, *75* (23), 7458–7471.

(78) Loring, J. S.; Thompson, C. J.; Zhang, C.; Wang, Z.; Schaef, H. T.; Rosso, K. M. In Situ Infrared Spectroscopic Study of Brucite Carbonation in Dry to Water-Saturated Supercritical Carbon Dioxide. *J. Phys. Chem. A* **2012**, *116* (19), 4768.

(79) Harrison, A. L.; Power, I. M.; Dipple, G. M. Accelerated Carbonation of Brucite in Mine Tailings for Carbon Sequestration. *Environ. Sci. Technol.* **2013**, *47* (1), 126–134. https://doi.org/10.1021/es3012854.

(80) Harrison, A. L.; Dipple, G. M.; Power, I. M.; Mayer, K. U. Influence of Surface Passivation and Water Content on Mineral Reactions in Unsaturated Porous Media: Implications for Brucite Carbonation and CO_2 Sequestration. *Geochim. Cosmochim. Acta* **2015**, *148*, 477.

(81) Zarandi, A. E.; Larachi, F.; Beaudoin, G.; Plante, B.; Sciortino, M. Multivariate Study of the Dynamics of CO_2 Reaction with Brucite-Rich Ultramafic Mine Tailings. *International Journal of greenhouse gas control* **2016**, *52*, 110–119.

(82) Boschi, C.; Dini, A.; Baneschi, I.; Bedini, F.; Perchiazzi, N.; Cavallo, A. Brucite-Driven CO_2 Uptake in Serpentinized Dunites (Ligurian Ophiolites, Montecastelli, Tuscany). *Lithos* **2017**, *288*, 264–281.

(83) Zarandi, A. E.; Larachi, F.; Beaudoin, G.; Plante, B.; Sciortino, M. Nesquehonite as a Carbon Sink in Ambient Mineral Carbonation of Ultramafic Mining Wastes. *Chemical Engineering Journal* **2017**, *314*, 160–168.

(84) Larachi, F.; Aksenova, D.; Yousefi, B.; Maldague, X. P. V.; Beaudoin, G. Thermochemical Monitoring of Brucite Carbonation Using Passive Infrared Thermography. *Chemical Engineering and Processing-Process Intensification* **2018**, *130*, 43–52.

(85) Rausis, K.; Ćwik, A.; Casanova, I. Phase Evolution during Accelerated CO_2 Mineralization of Brucite under Concentrated CO2 and Simulated Flue Gas Conditions. *Journal of CO_2 Utilization* **2020**, *37*, 122–133.

(86) Nguyen, H.; Santos, H.; Sreenivasan, H.; Kunther, W.; Carvelli, V.; Illikainen, M.; Kinnunen, P. On the Carbonation of Brucite: Effects of Mg-Acetate on the Precipitation of Hydrated Magnesium Carbonates in Aqueous Environment. *Cement and Concrete Research* **2022**, *153*, 106696.

(87) Dong, S.; Xing, T.; Zhao, L.; Zhu, C.; Yao, X.; Zhao, S.; Teng, H. H. Physical and Chemical Effects of H_2O on Mineral Carbonation Reactions in Supercritical CO_2. *Applied Geochemistry* **2023**, *155*, 105668.

(88) Campione, M.; Corti, M.; D'Alessio, D.; Capitani, G.; Lucotti, A.; Yivlialin, R.; Tommasini, M.; Bussetti, G.; Malaspina, N. Microwave-Driven Carbonation of Brucite. *Journal of CO_2 Utilization* **2024**, *80*, 102700.

(89) Back, J.; Ismailov, A.; Sreenivasan, H.; Smått, J.-H.; Santos, H. S.; Nguyen, H.; Levänen, E.; Zevenhoven, R.; Kinnunen, P. Influence of Additives, Temperature, and Pressure on the

Morphology of Nesquehonite– Results from Three Synthesis Routes. *emergent mater.* **2025**. https://doi.org/10.1007/s42247-024-00968-8.

(90) Yang, J.; Han, Y.; Luo, J.; Leifer, K.; Strømme, M.; Welch, K. Synthesis and Characterization of Amorphous Magnesium Carbonate Nanoparticles. *Materials Chemistry and Physics* **2019**, *224*, 301–307.

(91) Kuzmann, E.; Nagy, S.; Vértes, A. Critical Review of Analytical Applications of Mössbauer Spectroscopy Illustrated by Mineralogical and Geological Examples (IUPAC Technical Report). *Pure and Applied Chemistry* **2003**, *75* (6), 801–858. https://doi.org/10.1351/pac200375060801.

(92) Génin, J.-M. R.; Bourrié, G.; Trolard, F.; Abdelmoula, M.; Jaffrezic, A.; Refait, P.; Maitre, V.; Humbert, B.; Herbillon, A. Thermodynamic Equilibria in Aqueous Suspensions of Synthetic and Natural Fe(II)−Fe(III) Green Rusts: Occurrences of the Mineral in Hydromorphic Soils. *Environ. Sci. Technol.* **1998**, *32* (8), 1058–1068. https://doi.org/10.1021/es970547m.

(93) Refait, P. H.; Abdelmoula, M.; Génin, J.-M. Mechanisms of Formation and Structure of Green Rust One in Aqueous Corrosion of Iron in the Presence of Chloride Ions. *Corrosion Science* **1998**, *40* (9), 1547–1560.

(94) Kozlov, I.; Levshov, P. Amakinite, a New Mineral of the Brucitepyrochroite Group. *American Mineralogist* **1962**, *47*, 1218.

(95) Carlin, W.; Malvoisin, B.; Lanson, B.; Brunet, F.; Findling, N.; Lanson, M.; Magnin, V.; Fargetton, T.; Jeannin, L.; Lhote, O. FeIII-Substituted Brucite: Hydrothermal Synthesis from

802 ($Mg_{0.8}Fe^{II}_{0.2}$)-Brucite, Crystal Chemistry and Relevance to the Alteration of Ultramafic
803 Rocks. *Applied Clay Science* **2023**, *234*, 106845.

804 (96) Hewett, D. F.; Fleischer, M. Deposits of the Manganese Oxides. *Economic Geology* **1960**, *55*
805 (1), 1–55.

806 (97) Post, J. E. Manganese Oxide Minerals: Crystal Structures and Economic and Environmental
807 Significance. *Proceedings of the National Academy of Sciences* **1999**, *96* (7), 3447–3454.

808 (98) Post, J. E.; Heaney, P. J.; Ilton, E. S.; Elzinga, E. J. The Crystal Structure of Feitknechtite (β-
809 MnOOH) and a New MnOOH Polymorph. *American Mineralogist* **2023**, *108* (11), 2131–
810 2141. https://doi.org/10.2138/am-2022-8729.

811 (99) Shannon, R. D. Revised Effective Ionic Radii and Systematic Studies of Interatomic
812 Distances in Halides and Chalcogenides. *Foundations of Crystallography* **1976**, *32* (5), 751–
813 767.

814 (100) Zigan, F. Neutronenbeugungsmessungen Am Brucit. *Neues Jahrb. Mineral. Monatsh.*
815 **1967**, *4*, 137.

816 (101) Parise, J. B.; Leinenweber, K.; Weidnner, D. J.; Tan, K.; Von Dreele, R. B. Pressure-
817 Induced H Bonding: Neutron Diffraction Study of Brucite, $Mg(OD)_2$, to 9.3 GPa. *American*
818 *Mineralogist* **1994**, *79* (1–2), 193–196.

819 (102) Giester, G.; Lengauer, C. L.; Rieck, B. The Crystal Structure of Nesquehonite, $MgCO_3 \cdot$
820 $3H_2O$, from Lavrion, Greece. *Mineralogy and Petrology* **2000**, *70* (3–4), 153–163.
821 https://doi.org/10.1007/s007100070001.

(103) Chung, D. Synchrotron X-Ray Diffraction Studies of Reactions in the Mg-H_2O-CO_2 System: Mechanisms, Kinetics, and Reactivity. **2025**.